Construction and Building Materials 451 (2024) 138871

Contents lists available at ScienceDirect

Construction and Building Materials

journal homepage: www.elsevier.com/locate/conbuildmat

Synthesis of graphene from waste rubber powder based on flash joule heating method and its influence on the performance of cement mortar

Chengbin Wang [a,b], Bin Wang [a,b], Xinghua Su [a], Rui He [a,b,*]

[a] School of Materials Science and Engineering, Chang'an University, Xi'an 710064, China
[b] Shaanxi School-Enterprise Joint Research Center for Advanced Transportation Infrastructure Materials, Chang'an University, Xi'an 710018, China

ARTICLE INFO

Keywords:
Rubber-based graphene
Flash joule heating
Cement mortar
Mechanical properties
Microstructure

ABSTRACT

Due to the excellent strength, ultra-high specific surface area and extremely small size of graphene, it is an ideal modification component for cementitious materials. However, the conventional production methods of graphene are often time-consuming, energy-intensive, and expensive, which limits its development in cementitious materials to a certain extent. Recently, flash joule heating (FJH) has been shown to be an effective and green method to synthesize graphene. Therefore, the present paper attempts to prepare graphene from waste rubber powder by FJH and study its effect on the properties of cementitious materials. The results demonstrate that the study successfully converted waste rubber powder into multilayer graphene with minimal defects. Raman spectroscopy and XRD analyses revealed characteristic peaks of graphene, while the results of TGA show that graphene have excellent thermal stability. XPS analysis indicate that the purity of graphene can reach about 87.33 %. SEM and TEM reveal its multi-layered lamellar structure. Moreover, we synthesized graphene-enhanced cement mortar, which exhibited improved mechanical properties. The pore structure was optimized, with decreased porosity and mean pore size. Microscopically, the presence of graphene led to a denser arrangement of hydration products, fewer pores, and cracks. AFM results demonstrated that graphene effectively enhanced the average elastic modulus at the nanoscale interface. This study contributes to the advancement of sustainable development by recycling waste rubber and proving the potential of graphene in cement composites.

1. Introduction

With the rapid development of the automotive and rubber industries, a large amount of waste rubber products, including car tires, rubber gloves, rubber shoes, etc. are generated annually worldwide [1,2]. The commonly used methods for handling them include landfill, renovation and recycling, thermal utilization, and pyrolysis [3]. Among them, landfill is the most primitive disposal method. However, the landfill treatment will cause pollution to groundwater quality and surrounding soil [4]. Theoretically, renovation reduces the waste and has certain economic benefits, but in practice, renovated products have poor quality and safety. The thermal energy utilization is a valuable method for waste recovery [5]. After being shredded, waste tires can be mixed with other combustible waste to produce solid refuse-derived fuel, which can partially substitute coal. Compared to other waste fuels, it has the advantages of low moisture and ash content. However, the application of this technology is not widely spread. Thermal cracking is a thermochemical treatment that allows the decomposition of chemical bonds in compounds under non-oxidizing conditions (inert atmosphere or vacuum). From a recovery perspective, the main advantage of this method is that it can process waste and generate value-added products such as pyrolysis oil and carbon black [6]. However, this process consumes a significant amount of energy. Therefore, exploring more advanced methods for recycling waste rubber is of great importance.

In 2020, Luong et al. utilized a novel fast Joule heating technique (FJH) to convert low-value carbon sources such as coal, carbon black, biomass char, waste plastics, and rubber into high-value graphene [7–11]. In FJH process, direct current passes through the sample, and temperatures above 3000 K are generated within milliseconds. Such high temperature combined with an extremely fast heating rate allows for the volatilization of all elements except carbon in the sample, leading to the breaking and recombination of molecular bonds within the carbon-based material [12–14]. FJH overcomes the drawbacks of large-scale reaction equipment and slow heating rate associated with traditional heating methods. It provides a new approach to the top-down synthesis of graphene.

* Corresponding author at: School of Materials Science and Engineering, Chang'an University, Xi'an 710064, China.
E-mail address: heruia@163.com (R. He).

https://doi.org/10.1016/j.conbuildmat.2024.138871
Received 20 July 2024; Received in revised form 29 September 2024; Accepted 19 October 2024
Available online 26 October 2024

Graphene is a 2D nanomaterial composed of carbon atoms with a hexagonal lattice structure formed by sp^2 hybridized orbitals [15]. Due to its excellent strength and toughness, as well as its large specific surface area, it is often added to cement-based materials to improve properties [16,17]. Many scholars have conducted research on the reinforcement of cement-based materials with graphene. For example, He et al. [18] studied the influence of few-layer graphene (FLG) on the flowability, mechanical properties (compressive strength and flexural strength), and electrical properties of cement mortar. The experimental results showed that FLG can reduce the flowability of the mortar, improving its mechanical properties, and enhancing the electrical conductivity of cement mortar. Wang et al. [19] pointed out that graphene nanosheets facilitated the hydration of cement because more ion exchange occurred at early stages. Liu et al. [20] investigated the influence of multilayer graphene oxide (MGO) on the early mechanical properties and microstructure of cement mortar at low temperatures. They attributed the increase in mortar mechanical properties to the nucleation effect of MGO. Sheng et al. [21] optimized a surfactant for dispersing graphene, and found that the compressive strength and flexural strength at 28 days increased by 33.99 % and 27.18 %, respectively, when the graphene content was 0.03 %. Lu et al. [22] designed a new GO@Sand composite to improve the interface transition zone (ITZ) of cement mortar. Compared to ordinary cement mortar specimens, the compressive strength and flexural strength of mortar prepared with GO@Sand increased by 38 % and 44 % at 28 days. The improvement in mechanical properties is primarily attributed to the increased proportion of hydration products near the ITZ and a reduction in microstructural porosity.

Numerous studies have shown the great potential of graphene in the field of construction materials. However, its high cost and complex fabrication processes have hindered its widespread application. Therefore, a cost-efficiency method for preparing the graphene is eagerly needed. This study focuses on the utilization of inexpensive waste rubber powder for the production of high-value graphene using the FJH technique. In addition, the possibility of incorporating graphene (FG) into cement-based materials was then explored. It was found that FG exhibited an initial increase followed by a decrease in its influence on the mechanical properties of mortar compared to the control group. From a microstructural perspective, the porosity and structure of the cement mortar were measured, revealing that the introduction of FG can reduce the porosity and pore size of the mortar. The microstructural morphology of the FG-modified cement mortar was observed using scanning electron microscopy (SEM) to investigate the enhancement mechanism. Additionally, the surface topography, roughness, and elastic modulus of the FG-modified cement mortar's ITZ were characterized using atomic force microscopy (AFM). This study not only provides an effective pathway for the high-value utilization of waste rubber powder but also offers valuable insights for the green development of graphene in the construction industry. It is expected to address the challenges of graphene's high manufacturing costs and complex fabrication processes, thus expanding its application in cement-based materials.

2. Materials and methods

2.1. Materials and instrument

The rubber particles had a particle size ranging from 0.25 mm to 0.425 mm, supplied by the Xinlei Mineral Powder Factory in Shijiazhuang. As rubber was an insulator, 5 % carbon black (CB) was mixed into the rubber powder to enhance its conductivity, resulting in a uniform mixture known as rubber carbon black composite (RCB). The conductive carbon black powder used here is supplied by TIMCAL with a conductivity of 10–15 S/cm. The surfactant used to disperse the graphene was polyvinylpyrrolidone (PVP), supplied by the Shanghai Aladdin Biochemical Technology Co., Ltd, with a high purity and an average molecular weight of 1300000. The cement used for preparing mortar samples in this paper is P·O 42.5 ordinary Portland cement, which was produced by Wuxi Tianshan Cement Co., Ltd. The aggregates used were in accordance with ISO standards and were supplied by Xiamen ISO Standard Sand Co., Ltd.

The FJH reaction apparatus (FJH-400, Shenzhen Zhongke Jingyan Technology Co., Ltd.), comprised a multifunctional control system, vacuum chamber, vacuum pump, and temperature measurement system. The multifunctional control system had the capabilities of controlling the charge and discharge rate, selecting discharge modes, and measuring the sample resistance. The temperature measurement system utilized an ultra-high temperature infrared thermometer, with a temperature measurement range from 2000 K to 7000 K, and a measurement accuracy of ± 5 %. The equipment was equipped with a 128 mF capacitor and operates normally on standard 220 V AC power supply. The dispersing equipment used in the process of preparing graphene aqueous solution was the ultrasonic cell disruptor, model TL-1200Y, with a maximum power of 1200 W, purchased from Jiangsu Tianling Instrument Co., Ltd. The mixer used in the preparation of cement mortar was produced from Wuxi Building Materials Test Instrument and Equipment Factory, and the model was JJ-5. The equipment complied with JC/T681-2005 standard.

2.2. Methods

2.2.1. Preparation of FG

Fig. 1 illustrated the process of preparing and dispersing FG. 190 mg of powder and 10 mg of carbon black were weighed and placed in a mortar, thoroughly mixed to achieve homogeneity. The resulting mixture was then filled into a quartz tube, with both ends of the quartz tube sealed with graphite blocks. The quartz tube utilized in this experiment was a cylindrical tube with a length of 6 cm, diameter of 1.2 cm, and a thickness of 0.3 cm. The graphite blocks were approximately 0.8 cm in height, with a diameter slightly smaller than the quartz tube, allowing them to be sealed within the tube. The quartz tube containing the sample was sealed with electrodes at both ends. Discharge voltage was set to 150 V. Once the charging voltage reached to 150 V, the discharge was initiated. The current will pass through the sample instantaneously, causing the temperature to rise sharply to above 3000 K. When the voltage dropped to the specified level (10 V), the discharge was stopped. The resultant flash evaporated graphene was termed as one-time flash graphene (OFG). Recharge to 150 V and start the discharge again. At this point, the temperature will also rise to a temperature above 3000 K, which should be higher than the temperature achieved during the first flash. The graphene obtained under these conditions was referred to as two-time flash graphene (TFG). During the experimental process, it was discovered that the quartz tube, containing the sample, could undergo a maximum of two FJH treatments. Exceeding this limit would lead to the quartz tube being unable to withstand the high temperatures, resulting in its rupture and wastage of the sample.

2.2.2. Preparation of FG suspension

Typically, dispersion of graphene involved a combination of surfactants and ultrasonic dispersion. The surfactant used was PVP, and mass ratio of TFG-to-PVP mass ratio of was 1:1. Initially, magnetic stirring was employed for 15 min, followed by ultrasonic dispersion using a sonicator at a power setting of 800 W. Each ultrasonic cycle consisted of 1.5 s of ultrasonication and 2.5 s of rest, with a total dispersion time of 20 min.

2.2.3. Preparation of cement mortar specimen

Two types of cement mortar were prepared. The first type consisted of standard mortar test cubes measuring 40 mm × 40 mm × 160 mm, following ISO standards. Each set comprised 450 g of cement, 1350 g of standard sand, and 225 g of water. The test group involved the addition of 0, 0.02 %, 0.04 %, 0.06 %, 0.08 %, and 0.1 % of TFG to the respective

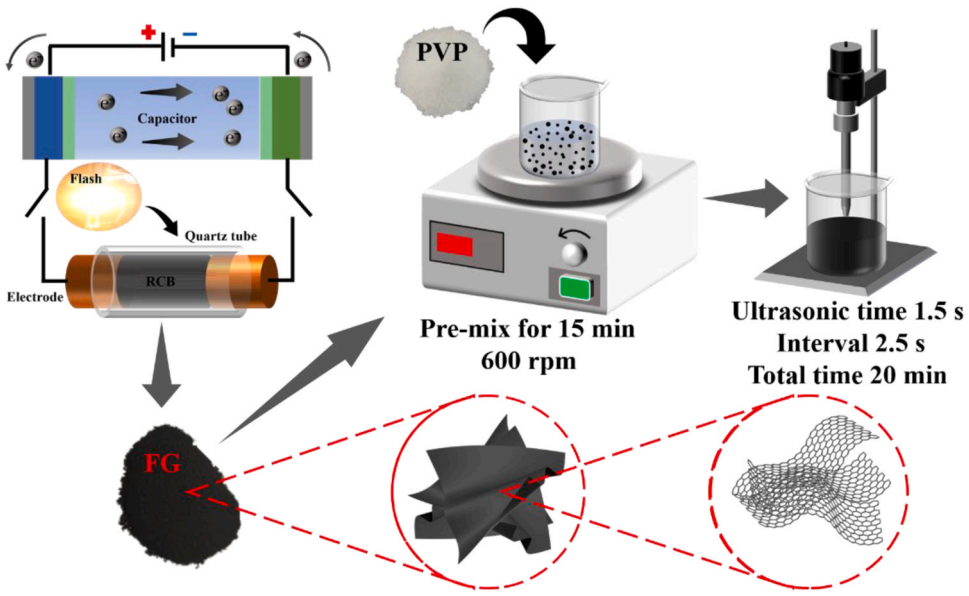

Fig. 1. Schematic diagram of the preparation of FG and FG dispersions.

cement masses. The specimen with no TFG was considered as the control group. The preparation of the TFG suspension was carried out following the method described in the previous section. Considering the dimensions required for pore analysis, specimens sized 100 mm × 100 mm × 100 mm were prepared, requiring 300 g of cement, 900 g of standard sand, 150 g of water, and the same TFG content as the first mortar type. The preparation process involved pouring the TFG suspension into a mixer, adding cement, and then stirring at low speed for 30 s. Starting at the second 30 s, standard sand was gradually added, followed by high-speed stirring for an additional 30 s. The mixer was then allowed to stand for 90 s, after which the mortar on the blades was scraped off. Finally, high-speed stirring was conducted for 60 s. The mortar was evenly poured into triplex molds, placed on a vibrating table to remove surface moisture, and demolded after 24 h, and then cured in a standard curing chamber for the corresponding age period.

2.3. Testing programme

2.3.1. Testing items of FG

Raman spectroscopy was performed on a laser confocal micro-Raman spectrometer with LabRAM Odyssey model (Japan Horiba LabRAM HR Evolution). A small amount of the sample was placed on a glass slide, and it was subjected to focused irradiation from a laser with a wavelength of 532 nm, delivering an output power of 100 mW. The scanning range was set between 1000 cm^{-1} and 3000 cm^{-1}. X-ray powder diffraction (XRD) was con-ducted using a D8 ADVANCE (Germany Bruker) with Cu Kα (λ = 1.54178 Å) radiation at room temperature and the data was collected from 5° to 90° with a scan rate of 2°/min to obtain phase structure of FG. The scan step size was 0.02°, 0.5 s per step. Thermogravimetric Analysis (TGA) data was collected using Mettler-TGA2 (Switzerland) at temperatures ranging from 50 °C to 1000 °C with a constant rate of 15 ℃/min. All sample tests were carried out in an air atmosphere. X-ray photoelectron spectroscopy (XPS, American Thermo Scientific K-Alpha) was used to analyze the elemental composition and relative content of the produced FG. The voltage of the X-ray source was 16KV and the current was 14.9 mA. SEM (Germany ZEISS, Sigma 300) was employed for the micro-morphological analysis of FG. An acceleration voltage of 5 kV was used. Transmission electron microscopy (TEM, JEOL JEM-F200, Japan) with an acceleration voltage of 200 kV was employed to characterized the FG. Prior to testing, FG was dissolved in water and subjected to ultrasonic treatment. Subsequently, the FG suspension was droplet-deposited onto a carbon grid and air-dried.

2.3.2. Testing items of FG modified cement mortar

The compressive strength and flexural strength of cement mortar at 3 d, 7 d and 28 d were determined by the TYE-300E compressive and flexural testing machine produced by Wuxi Jianyi Instrument & Machinery Co., Ltd. Three specimens at each age were tested, and the average of the three measurements was taken as the final strength.

SEM (Sigma 300) was employed for the micro-morphological analysis of FG-modified cement mortar. A small amount of sample was taken and glued directly to the conductive adhesive and sprayed with gold using the Oxford Quorum SC7620 sputter coater for 45 s before being tested. An acceleration voltage of 5 kV was used.

The analysis of pore structure was primarily conducted using the Rapid Air pore structure analyzer, model Rapid Air 457. Prior to pore structure analysis, the cured 28-day cubic mortar specimens were cut into thin slices measuring 100 mm × 100 mm × 20 mm. These slices were then sequentially polished using emery papers of 240, 280, 320, 360, and 400 mesh. Subsequently, the specimens were cleaned with anhydrous ethanol using an ultrasonic cleaning machine for 10 min to remove any surface powder. After cleaning, the specimens were dried and their surfaces were blackened using carbon ink. Once the ink was dry, a calcium carbonate slurry was applied to the surface, and any excess slurry was removed by scraping, completing the specimen preparation. The surface views of the specimen obtained according to the above preparation process was shown in Fig. 2.

The QNM mode of AFM, Germany Bruker was used to obtain information pertaining to the morphology, roughness, and Young's modulus of FG-modified cement mortar. The scanning resolution was set at 256 × 256, the scanning frequency at 0.5 Hz, and the scanning area at 20 μm × 20 μm. Given the high requirements for the surface roughness of the sample in AFM, pretreatment was conducted on the mortar. Firstly, the mortar was cut into small thin slices of around 2 cm × 2 cm × 0.5 cm using a cutting machine. Subsequently, it was then coarsely ground using sandpapers of 240, 280, 320, 360, and 400 mesh respectively for 5 min at each level, and subsequently polished with diamond sandpapers of 9 μm, 5 μm, 3 μm, and 1 μm using a polishing machine at a rotating speed of 150 r/min for 5 min at each level. Lastly, the sample was cleaned with an ultrasonic cleaning machine using anhydrous ethanol and sonicated for 10 min before air-drying for further usage.

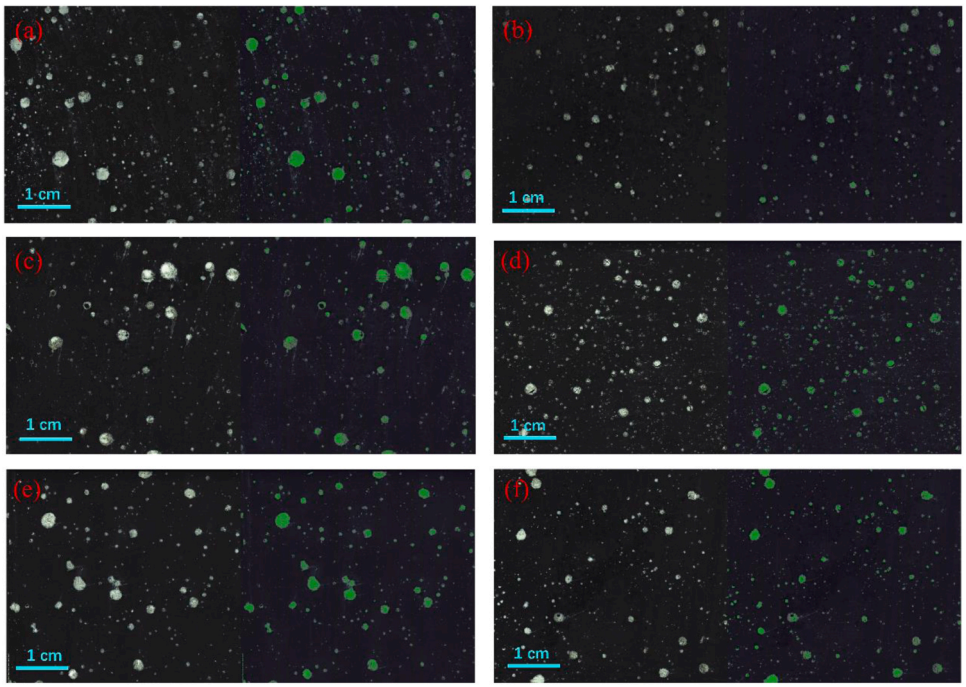

Fig. 2. Surface views of mortar evaluated with Rapid Air for pore distribution characteristics, (a–f) FG contents are 0 %, 0.02 %, 0.04 %, 0.06 %, 0.08 %, and 0.1 %, respectively.

3. Results and discussion

3.1. Process analysis of flash joule heating

FJH is a process of electric field-assisted heating. Firstly, the capacitor is charged, and after the charging process is completed, the discharge begins. During the discharge process, the capacitor acts as a power source and forms a circuit with the sample, releasing the charge in the capacitor to flow through the sample. Thus, high temperatures are obtained due to Joule heating. High temperatures can purify the carbon element in the rubber powder, resulting in a high purity FG. Fig. 3 shows the temperature-time curve of the Joule heating process. Stage I represents the first discharge process. The highest temperature approximately 3200 K can be reached at around 0.9 s. The stage II is the charging stage, which has no impact on the heating of the Joule process. The third stage is the second discharge. Through multiple experiments, we found that after the Joule heating treatment, the sample resistance generally falls below 10 Ω. This phenomenon is similar to the flash sintering [23,24]. Many researchers believe that flash sintering is driven by Joule heating, which can promote the diffusion of substances. As the Joule heating proceeds, the degree of carbonization in the sample gradually increases, leading to an increase in the sample's electrical conductivity, and the occurrence of intense flashing as a result of thermal radiation [25–27]. Similarly, in multiple experiments, we found that the temperature in the third stage is generally higher than that in the first stage, and the samples obtained after two Joule heating treatments are more uniform than those treated only once. The following equation is used to calculate the energy required for the FJH process:

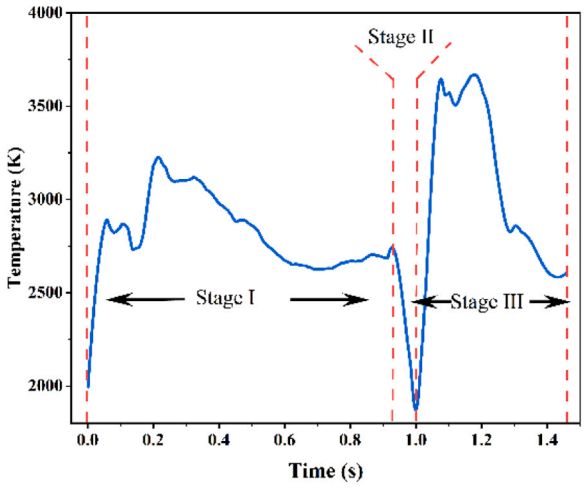

Fig. 3. Temperature curve in FJH process.

$$E = \frac{(V_1^2 - V_2^2) \times C}{2 \times M} \quad (1)$$

where E represents energy, V_1 represents initial voltage, V_2 represents final voltage, M represents the mass of the sample, and C represents the capacitance of the capacitor [7]. The initial voltage was set to 150 V, and the discharge was terminated when the voltage dropped to 10 V. According to Formula (1), the energy consumption for FJH was calculated to be approximately 7.17 kJ/g = 1.99 kWh/kg. In Xi'an, Shaanxi Province, the electricity price is ¥0.4983/kWh, the cost in electricity to convert 1 kg of RCB into OFG and TFG is about ¥0.99 and ¥1.98 separately, which is far cheaper than traditional production methods of graphene. So, FJH has certain economic and ecological benefits.

3.2. Characterization and evaluation of FG

Raman spectroscopy is commonly used to characterize graphene. For carbon materials with sp^2 hybridization, typical D, G, and 2D peaks are usually present. From Fig. 4(a), it can be observed that both OFG and TFG exhibit characteristic peaks of graphene. The G peak is the main feature peak of graphene, arising from in-plane vibrations of sp^2 carbon atoms, typically appearing near 1580 cm^{-1}, and can reflect the layer number of graphene. The D peak is generally considered as the peak of disordered vibrations in graphene, which is used to characterize structural defects in graphene and typically appears around 1350 cm^{-1}. The 2D peak, also known as the G′ peak, is used to characterize the stacking

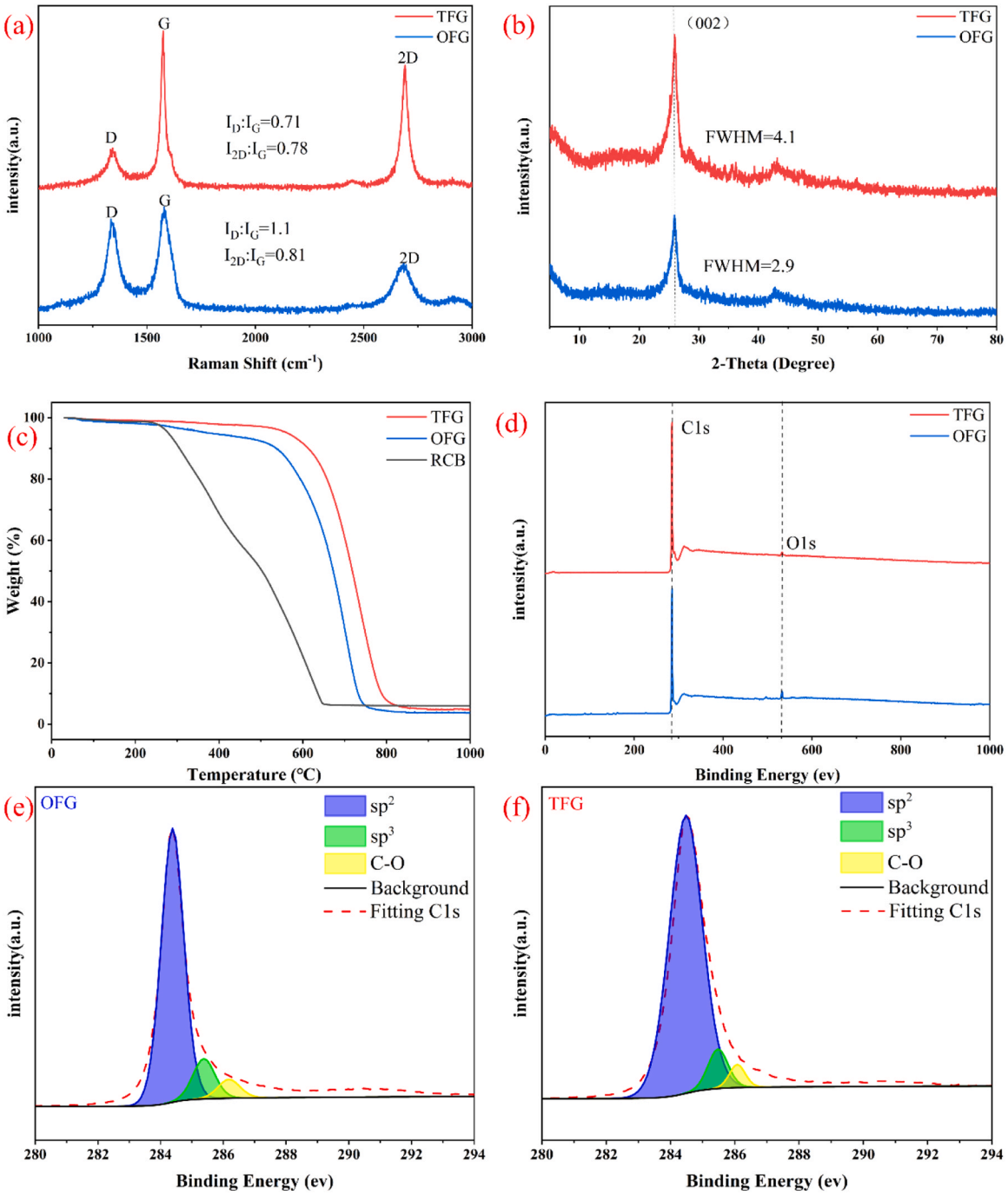

Fig. 4. (a) Raman spectra of FG; (b) XRD profile of FG; (c) TGA profile of FG; (d)XPS profile of FG; (d, e) C1s peak profile of FG.

of carbon atoms in graphene, typically appearing near 2700 cm^{-1} [28]. Generally, a lower I_D/I_G implies fewer defects [29], and the instantaneous high temperature and rapid heating rate of FJH generate some disordered structures and defects in RCB into sp^2 hybridized structures. TFG shows a reduced I_D/I_G compared to OFG, decreasing from 1.1 to 0.71. This implies that under a fixed discharge voltage, the more times the sample is treated by FJH, the fewer defects of FG will be obtained, leading to higher quality. The full width at half maximum (FWHM) of the 2D peak can reflect information about the layers of graphene. As the number of graphene layers increases, the FWHM becomes wider. Through fitting calculations, the FWHM of OFG is approximately 109.18, while that of TFG is approximately 40.85, indicating that TFG has relatively fewer layers. Similarly, I_{2D}/I_G also reflects information about the layers of graphene. Generally, graphene with I_{2D}/I_G less than 1 has more than three layers [30,31]. The ratio obtained for OFG and TFG is similar and less than 1, indicating that their layers are both greater than three, roughly estimated to be between 5 and 7 layers based on the morphology images.

XRD can be used to analyze the degree of graphitization of FG. From Fig. 4(b), it can be seen that after FJH treatment, the sample exhibits a sharp (002) diffraction peak at 26.1°, indicating a good graphitization effect of the rubber powder after FJH treatment. Additionally, the FWHM width of the (002) plane diffraction gradually increases with an increase in the number of electrification cycles, indicating that increasing the number of electrification cycles, not only reduce the surface defects of FG, but also reduce the FG layers [32], which is

consistent with the results obtained from Raman spectroscopy.

The TGA test can be used to judge the organic composition and thermal stability of the samples. As shown in Fig. 4(c), when the temperature rises from room temperature to 250 ℃, the non-carbon components in RCB begin to decompose, resulting in a gradual decrease in its mass. At this time, the masses of OFG and TFG basically remain unchanged. When the temperature rises to 600 ℃, RCB is almost completely consumed, while the masses of OFG and TFG begin to decrease rapidly. During the synthesis of FG by FJH, the instantaneous high temperature causes all volatiles in RCB to pyrolyze. The amorphous carbon structure has been transformed into a relatively stable graphene structure. In addition, the carbon pyrolysis temperature of TFG is higher than that of OFG, indicating that multiple FJH treatments make TFG have higher purity and better structural stability.

XPS is further utilized to analyze the phase composition of FG. As depicted in Fig. 4(d), the FJH-treated FG contains only carbon elements and trace amounts of oxygen elements, while sulfur and other impurity elements present in the rubber are eliminated. The relative content of oxygen in OFG is 6.45 %, and the relative content of carbon is 93.55 %. After undergoing consecutive FJH treatments, the relative content of carbon and oxygen in the resulting TFG changes to 98.8 % and 1.12 %, respectively. Following peak-fitting of the fine spectrum of carbon elements, it was discovered that the proportion of sp^2 hybridized carbon atoms in OFG is the highest, at approximately 82.56 %, with the remainder comprising sp^3 hybridized carbon atoms and C—O bonds. The proportion of sp^2 hybridized carbon atoms in TFG is approximately 88.84 %, with the remainder comprising sp^3 hybridized carbon atoms and C—O bonds. A preliminary estimation suggests that the purity of TFG after FJH treatment is around 87.33 %, while the purity of OFG is approximately 77.23 %, indicating an increase in purity of about ten percentage points. This also indicates that the more cycles of FJH treatment the sample undergoes, the more it promotes the generation of sp^2 hybridization [33,34].

3.3. Microscopic topography of FG

The microscopic morphologies of OFG and TFG were observed and analyzed using SEM and TEM. As shown in Fig. 5(a, b), OFG does not exhibit the traditional graphene nanoplate-like structure, but rather presents a structure similar to "stalactite stone". Nevertheless, OFG still exhibits the Raman characteristics of graphene, as confirmed by TEM images in Fig. 5(e, f). The SEM images in Fig. 5(c, d) of TFG demonstrate a markedly different multi-layer graphene nanoplate-like structure compared to OFG. The graphene sheets of three layers or more intertwine and stack together, consistent with the earlier estimation from I_{2D}/I_G, suggesting that TFG has more than three layers. The TEM images in Fig. 5(g, h) reveal the typical graphene nanoplate-like structure of TFG, and at a higher magnification, lattice stripe-like structures which are not observed in OFG are visible, indicating higher crystallinity of TFG. Through calculations, the lattice spacing of TFG is estimated to be approximately 0.37 nm.

The stark contrast in morphology between OFG and TFG can be attributed to the effect of FJH. Initially, the pristine sample consists of 95 % rubber powder and 5 % CB, with a high initial resistance, and the uneven distribution of the conductive phase CB leads to unstable electrical current flow through the sample. Despite achieving temperatures above 3000 K, the rapid heating action weakens, causing the amorphous carbon to transform into "stalactite" graphene. After one round of FJH treatment, the resistance of the sample reduces to within 10 Ω, greatly enhancing its conductivity and stability of current flow, shortening heating-up time, and increasing the maximum temperature, thereby transforming the original stalactite-like graphene into multi-layer stacked graphite nanoplates. The differences in the morphology of the two types of FG are reflected in the Raman spectrum, with OFG exhibiting a stronger D peak, indicating a higher density of crystal defects. In contrast, TFG shows a relatively lower D peak, suggesting a higher proportion of plate-like graphene nanoplates and fewer defects. This multi-layered graphene structure is more conducive to peeling off single-layer graphene and easier dispersion, making it more suitable as a reinforcing phase in cement-based materials.

3.4. Effect of FG content on mechanical properties of cement mortar

Using the method mentioned in Section 2.2.3, TFG was prepared into a suspension and used to fabricate standard cement mortar cubes measuring 40 mm × 40 mm × 160 mm, which were then cured under standard curing conditions. Compressive and flexural strength tests were performed on the cubes at 3, 7 and 28 days. As shown in Fig. 6, the strength initially increased and then decreased with increasing FG content. When the TFG content was 0.04 %, the mortar exhibited the highest strength, with compressive strengths of 29.8 MPa, 34.9 MPa and 49.5 MPa and flexural strengths of 3.4 MPa, 3.9 MPa and 7.8 MPa at 3, 7 and 28 days, respectively. Compared to the reference group, the strength was improved by 13.1 %, 7.4 % and 14.2 % for compressive strength

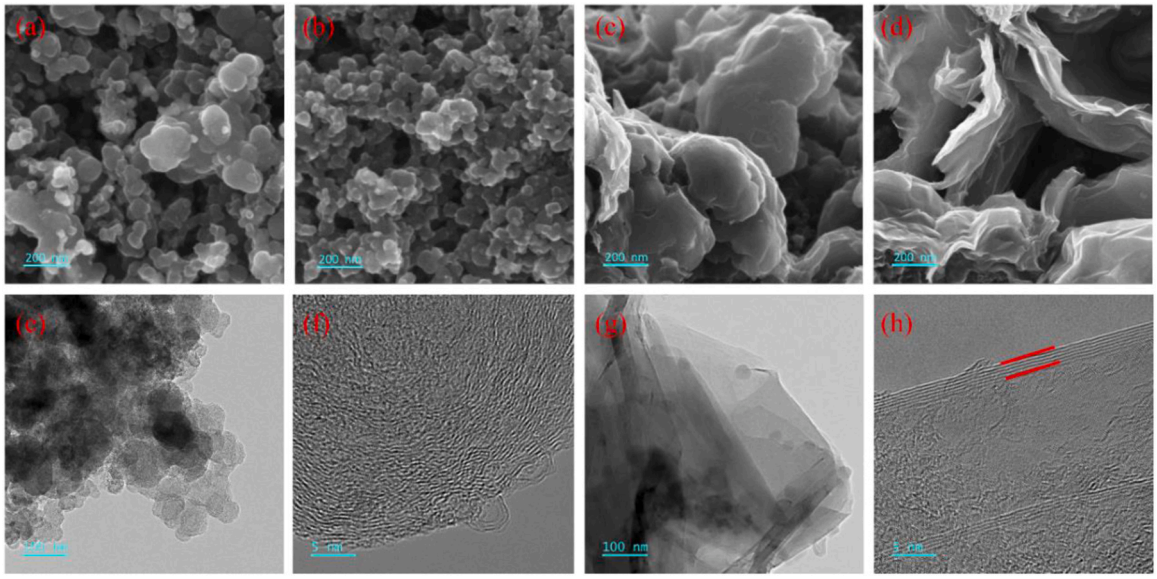

Fig. 5. (a, b) SEM images of OFG; (c, d) SEM images of TFG; (e, f) TEM image of OFG; (g, h) TEM image of TFG.

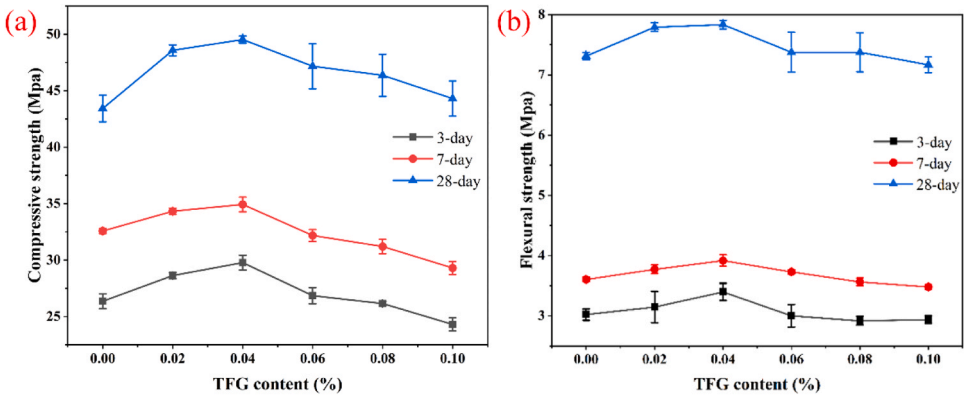

Fig. 6. The mechanical properties of cement mortar with different ages and varying graphene oxide content were investigated. (a) Compressive strength; (b) Flexural strength.

and 13.3 %, 8.3 % and 6.8 % for flexural strength, respectively. This is mainly due to the excellent mechanical properties of FG and its role in limiting crack propagation. When the TFG content increased from 0.04 % to 0.1 %, there was a slight overall decrease in flexural and compressive strength at different ages. This may be attributed to the influence of van der Waals forces between excess TFG, resulting in agglomeration of TFG within the cement mortar, which is detrimental to the formation and morphology of cement hydration products. Hindered by the TFG, the cement hydration products cannot bond well together, resulting in a decrease in the mechanical strength of the mortar [35,36].

3.5. *Effect of FG on the pore structure of cement mortar*

The air pore structure of cement mortar with different TFG contents was analyzed using a Rapid Air 457 hardened concrete air pore analyzer. The air content and average air pore diameter of hardened cement mortar with varying TFG contents are shown in Fig. 7(a). The air pores contents of mortar with 0 %, 0.02 %, 0.04 %, 0.06 %, 0.08 %, and 0.1 % TFG were 2.15 %, 1.38 %, 1.96 %, 2.02 %, 2.21 %, and 1.91 %, respectively. And the correspondingly average pore diameter are 0.094 mm, 0.083 mm, 0.076 mm, 0.094 mm, 0.1 mm, and 0.094 mm, respectively. The results indicate that, compared to the control group, the air pore content and average air pore diameter show a decreasing trend followed by an increasing trend with increasing TFG content. This suggests that TFG has a certain filling effect on the pores of cement mortar. However, when the concentration of TFG is too high, its dispersion becomes difficult, leading to agglomeration in the matrix, which results in an increase in air pore content and air pore diameter.

Fig. 7(b, c) respectively illustrate the size distribution of air pores in mortar with different TFG contents. It is evident from the figures that the

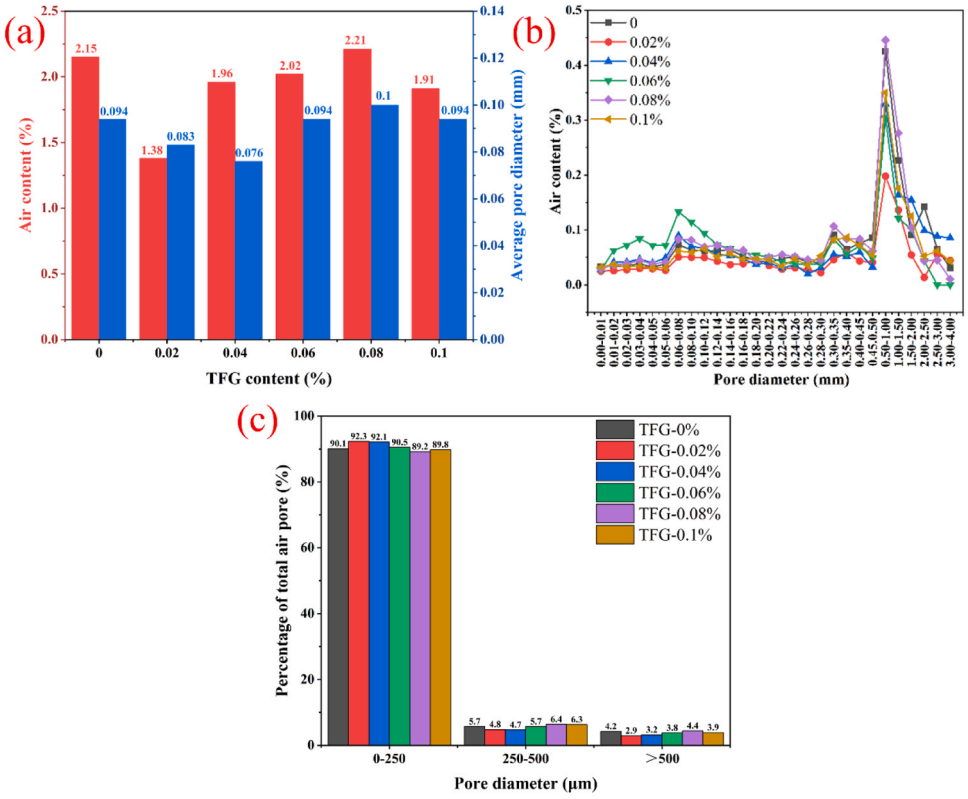

Fig. 7. (a) Air content and average pore diameter of hardened mortar with different TFG content; (b–c) Pore diameter distribution of hardened mortar with different TFG content.

majority of the air pores in the mortar are distributed in the range of 0–250 μm, constituting around 90 % of the total. The addition of TFG significantly alters the proportion of pore diameter in the mortar. Upon adding 0.02 % TFG, the air pores noticeably refine, with an increased proportion of pore in the 0–250 μm range and a decrease in pore larger than 500 μm. As the TFG content gradually increases from 0.02 % to 0.1 %, the proportion of 0–250 μm pores first increases and then decreases, while the proportion of pore diameter than 500 μm exhibits the opposite trend, decreasing initially and then increasing. This indicates that an appropriate TFG content can refine the air pore and improve the pore structure. When the TFG content reaches 0.08 %, the proportion of 0–250 μm pores is 89.2 %, lower than that of the control group, while the proportion of pore diameter than 500 μm is higher than that of the control group, indicating that excessive TFG content can have an adverse effect on the pore structure of the mortar.

3.6. Study on the microstructure of FG modified cement mortar

To investigate the influence of TFG on the microstructure of mortar, the morphological characteristics of the hydration products of cement mortar after 28 days of curing, with and without the addition of 0.04 % TFG, were observed using SEM. The microstructure of the hydration products of ordinary mortar after 28 days of curing is shown in Fig. 8 (a–c), revealing wide cracks and some micrometer-scale pores. Numerous needle-like and rod-like ettringite (AFt) are interspersed within the pores, with various hydration products distributed disorderly and poorly interconnected, resulting in an insufficiently dense structure. Fig. 8(d–f) depicts the cement mortar with 0.04 % TFG, demonstrating a noticeable increase in cement hydration products, characterized by regular and orderly crystalline shapes and aggregated structures, as well as a uniform and dense distribution. The presence of pores and cracks is significantly reduced, and various hydration products are encompassed and well connected to each other. This is attributed to the layered structure of TFG, which provides a large surface area and acts as a template during the cement hydration process, serving as nucleation sites and promoting cement hydration by attracting the preferential accumulation of active substances from the cement on the TFG. Additionally, when cracks occur, the sheet-like TFG tightly inserts into the cement matrix, impeding crack propagation. These microstructural changes are reflected in the improvement of the mechanical properties [18].

3.7. Nano-characterization of FG-modified cement mortar ITZ

The QNM technique implemented by the PeakForce Tapping mode has high demands for surface roughness of the samples. As the sample surface is directly in contact with the tip, insufficient smoothness may result in scratches on the sample surface. Therefore, a smooth surface is particularly important for obtaining accurate and reproducible morphological information and mechanical properties of the tested area [37]. In order to accurately determine the elastic modulus of the ITZ, the scanning area was selected near the aggregate, with a scanning range of 20 μm × 20 μm. The 3D topography of the sample, as shown in Fig. 9, revealed the rougher portion on the left as the ITZ, consistent with the morphology observed in reference [38,39], while the right side represented the aggregate. Roughness tests conducted on the ground sample

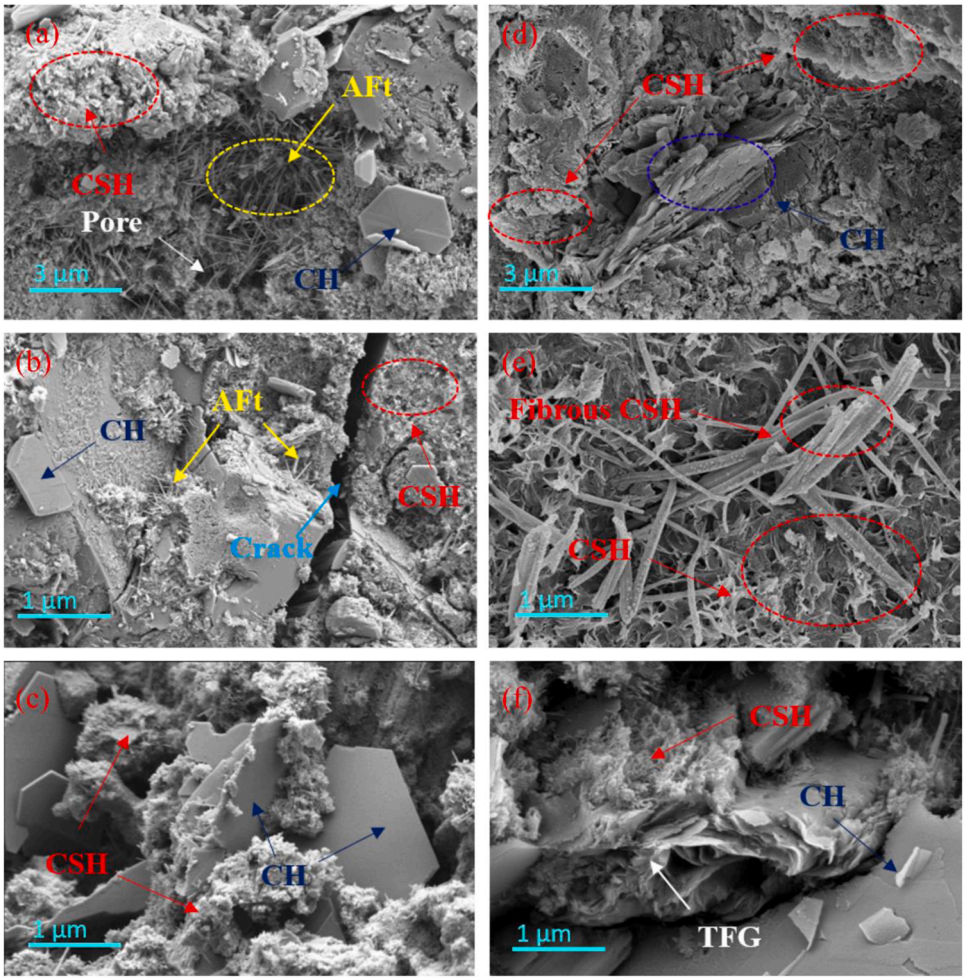

Fig. 8. Microscopic morphology of cement mortar; (a–c) Cement mortar without TFG addition; (d–f) Cement mortar with 0.04 % TFG addition.

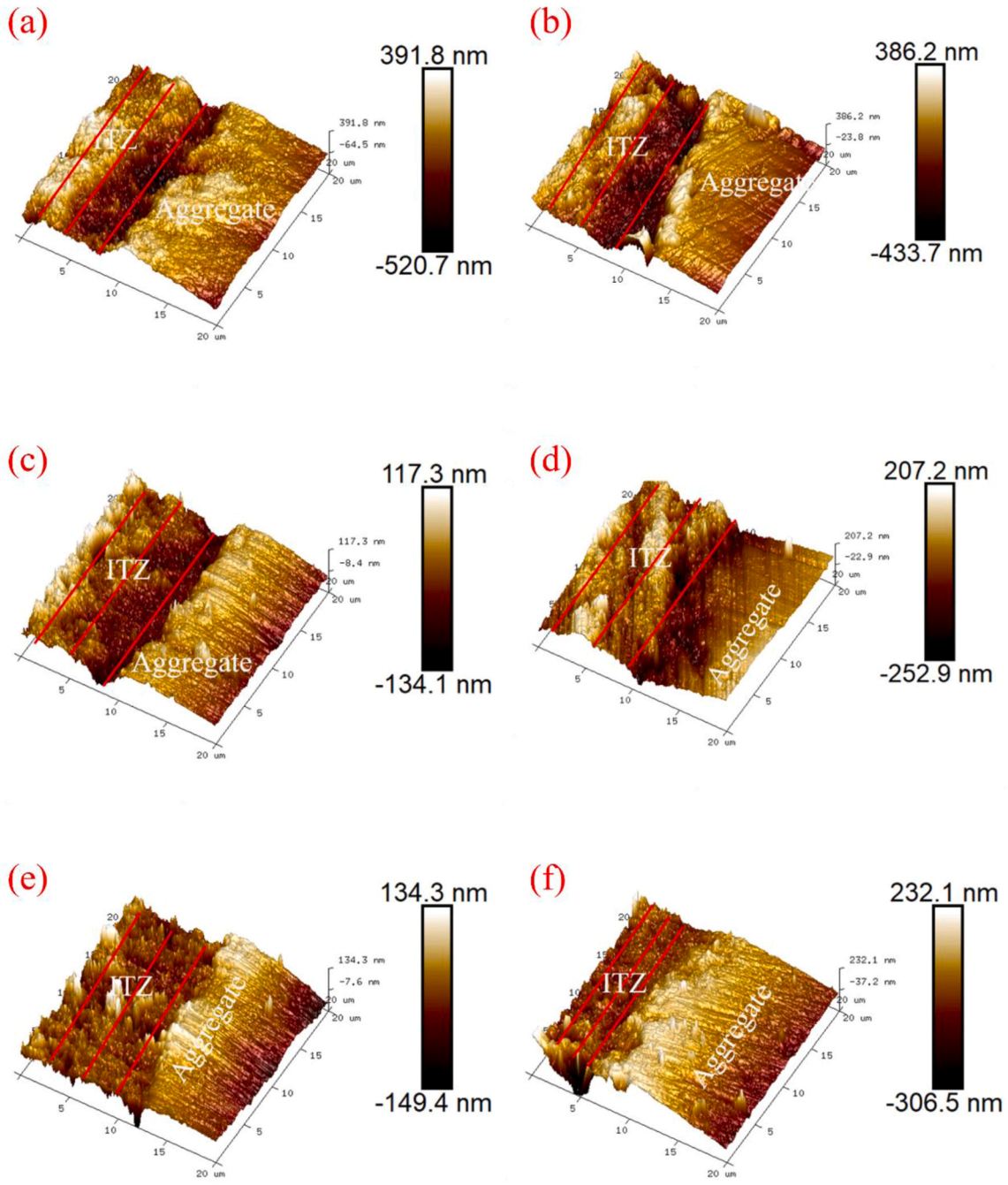

Fig. 9. (a–f) AFM 3D topography image of TFG modified cement mortar, with TFG content of 0 %, 0.02 %, 0.04 %, 0.06 %, 0.08 %, and 0.1 %.

within the selected range yielded the results shown in Table 1, where Ra represents the arithmetic mean and RMS represents the root mean square. Although the influence of the addition of fine-grained materials on the roughness of cement mortar cannot be discerned from the data, these values are sufficient to support AFM-QNM testing.

Table 1
Roughness of samples based on AFM tapping test.

Content of TFG (%)	*Ra* (nm)	*RMS* (nm)
0	81.4	99.2
0.02	97	122
0.04	29.5	36.3
0.06	50.4	64.8
0.08	30.6	39.5
0.1	58.6	74.1

Using AFM-QNM technique, the overall elastic modulus of all samples was tested. Fig. 10(a–f) all exhibit the same trend, starting with a stable range, followed by rapid growth, and eventually reaching a plateau. This is because the elastic modulus of the aggregate is higher than that of the ITZ. The RMS values of the elastic modulus for ITZ in all samples are shown in Table 2. The elastic modulus of ITZ in the control group is only 3.14 GPa. When the TFG content is between 0.02 % and 0.1 %, the elastic modulus of the ITZ increases by 72.3 %, 93.3 %, 67.2 %, 71 %, and 40.4 % compared to the control group, respectively.

Further analysis was carried out within the ITZ, with three random lines drawn for data extraction. The obtained scatter plot in Fig. 11 depicts the root mean square of the elastic modulus, with the red line representing the trend. The RMS value for the control group sample is 3.78 GPa, while the addition of TFG significantly increased this value. The elastic modulus values for mortar with TFG content between 0.02 %

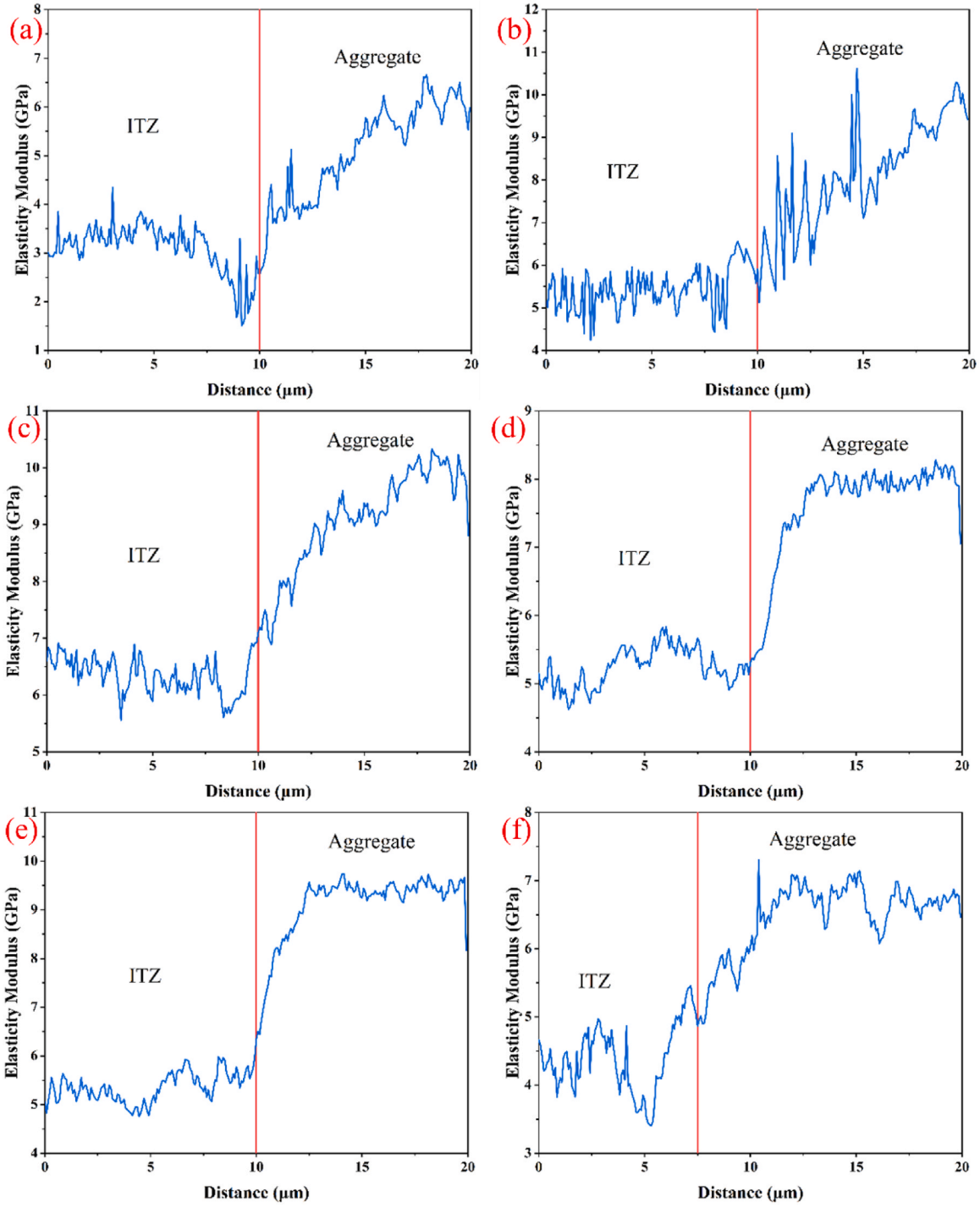

Fig. 10. (a–f) Line chart of the elasticity modulus of TFG-modified cement mortar obtained from QNM testing, with TFG content of 0 %, 0.02 %, 0.04 %, 0.06 %, 0.08 %, and 0.1 %.

Table 2
Elastic modulus of samples based on AFM test.

Content of TFG (%)	Calculation range (μm)	*RMS* (GPa)
0	0–10	3.14
0.02	0–10	5.41
0.04	0–10	6.07
0.06	0–10	5.25
0.08	0–10	5.37
0.1	0–7.5	4.41

and 0.1 % were 5.69 GPa, 6.48 GPa, 5.5 GPa, 5.89 GPa, and 4.88 GPa, respectively, indicating the corresponding increase of 50.5 %, 71.4 %, 45.5 %, 55.8 %, and 29.1 %. These research findings demonstrate that the addition of TFG does indeed enhance the elastic modulus of the ITZ.

Microscopic analysis and research are beneficial for a better understanding of the strengthening mechanism of TFG in cement mortar. Pore structure testing shows that TFG can reduce the number of pores in the mortar and optimize their size distribution, resulting in a denser matrix. SEM observations reveal a well-organized distribution of hydration products, closely connected to each other, and a reduction in cracks. All of these can be attributed to the layered structure of TFG, which

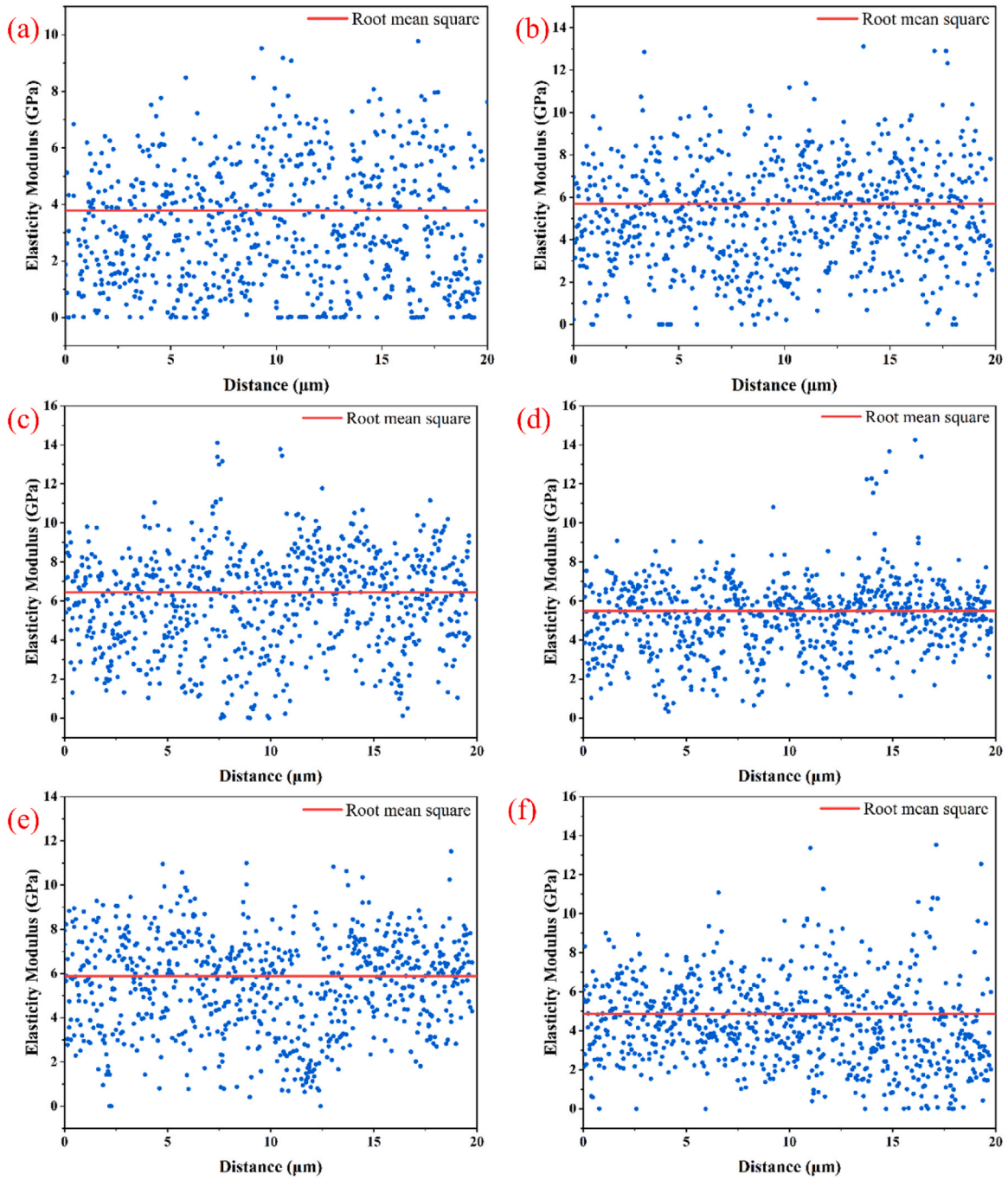

Fig. 11. (a–f) Elastic modulus scatter chart ITZ obtained from QNM testing, with TFG content of 0 %, 0.02 %, 0.04 %, 0.06 %, 0.08 %, and 0.1 %.

provides reactive sites for hydration reactions, thereby promoting more complete hydration. The ITZ has a significant impact on the strength and durability of cement-based materials, as its relatively lower strength makes it prone to failure [40]. Conclusions drawn from the elastic modulus of the ITZ measured by AFM indicate that TFG can greatly improve the elastic modulus of the ITZ, and a higher elastic modulus signifies greater deformation resistance. The enhancement of these microscopic structures by TFG is manifested macroscopically as improved mechanical properties.

4. Conclusions

In this study, low-defect multilayered graphene sheets are successfully prepared from the rubber powder using the FJH technique, without the addition of any chemical reagents or pretreatment. Subsequently, TFG is formulated into an aqueous solution and used as a reinforcement phase in cement mortar. The various properties of TFG-modified cement mortar are analyzed, and the results shows that:

(1) The Raman spectra of both OFG and TFG shows graphene characteristic peaks, but TFG shows a lower I_D/I_G ratio. The presence of the (002) characteristic peak in the XRD image demonstrates the high graphitization of graphene. The results of TGA prove the excellent thermal stability of FG. According to the test results of XPS, the purity of TFG and OFG is about 87.33 % and 77.23 %, respectively. SEM and TEM analysis demonstrate that the prepared TFG in this study has a typical layered structure of graphene nanosheets.

(2) TFG can enhance the mechanical properties of cement mortar. With the increase of TFG content, the mechanical properties initially increase and then decrease. The highest strength is achieved with a TFG content of 0.04 %, resulting in a 14.2 % increase in compressive strength and a 6.8 % increase in flexural strength after 28 days.
(3) The macroscopic increase in strength is the result of the microscopic action of the TFG. Due to the ultra-high specific surface area and extremely small size of TFG, the addition of TFG not only reduces the total pore content and pore size of the mortar, but also reduces the cracks inside the mortar, making the connection between its hydration products tighter.
(4) AFM-QNM testing results shows that TFG can enhance the elastic modulus of the ITZ at the nanoscale. The root mean square values of the ITZ are determined using two different calculation methods. Compared to the elastic modulus of the ITZ in ordinary cement mortar, the addition of 0.04 % TFG result in a respective increase in the elastic modulus of 93.3 % and 71.4 %.
(5) FJH can provide a new avenue for the utilization of low-value waste rubber, turning "black pollution" into a valuable resource. Furthermore, it has the potential to streamline the traditional graphene production processes, thus reducing the production costs of graphene and expanding its application in cement-based materials.

CRediT authorship contribution statement

Chengbin Wang: Writing – original draft, Methodology, Investigation, Data curation. **Bin Wang:** Investigation, Formal analysis. **Xinghua Su:** Writing – review & editing, Conceptualization. **Rui He:** Writing – review & editing, Resources, Methodology.

Declaration of Competing Interest

The authors declare that they have no known competing financial interests or personal relationships that could have appeared to influence the work reported in this paper.

Acknowledgements

The research was supported by the National Natural Science Foundation of China (No. 52278429), Key R&D Project in Shaanxi Province (Nos. 2023-ZDLGY-25, 2023-YBGY-495), the Fundamental Research Funds for the Central Universities,-CHD (No. 300102312402), Transportation Science and Technology Project in Shaanxi Province (Nos. 21-50K, 23-22K, 23-91K, 24-14K).

Data availability

Data will be made available on request.

References

[1] P.T. Williams, Pyrolysis of waste tyres: a review, Waste Manag. 33 (8) (2013) 1714–1728, https://doi.org/10.1016/j.wasman.2013.05.003.
[2] K. Januszewicz, P. Kazimierski, T. Suchocki, D. Kardas, W. Lewandowski, E. Klugmann-Radziemska, J. Luczak, Waste rubber pyrolysis: product yields and limonene concentration, Materials 13 (19) (2020), https://doi.org/10.3390/ma13194435.
[3] A.A. Yehia, Recycling of rubber waste, Polym.-Plast. Technol. Eng. 43 (6) (2004) 1735–1754, https://doi.org/10.1081/ppt-200040086.
[4] B. Rijo, A.P.S. Dias, L. Wojnicki, Catalyzed pyrolysis of scrap tires rubber, J. Environ. Chem. Eng. 10 (1) (2022), https://doi.org/10.1016/j.jece.2021.107037.
[5] S.Y. Leong, S.Y. Lee, T.Y. Koh, D.T.C. Ang, 4R of rubber waste management: current and outlook, J. Mater. Cycles Waste Manag. 25 (1) (2023) 37–51, https://doi.org/10.1007/s10163-022-01554-y.
[6] W.W. Han, D.S. Han, H.B. Chen, Pyrolysis of waste tires: a review, Polymers 15 (7) (2023), https://doi.org/10.3390/polym15071604.
[7] D.X. Luong, K.V. Bets, W.A. Algozeeb, M.G. Stanford, C. Kittrell, W. Chen, R. V. Salvatierra, M.Q. Ren, E.A. McHugh, P.A. Advincula, Z. Wang, M. Bhatt, H. Guo, V. Mancevski, R. Shahsavari, B.I. Yakobson, J.M. Tour, Gram-scale bottom-up flash graphene synthesis, Nature 577 (7792) (2020) 647–651, https://doi.org/10.1038/s41586-020-1938-0.
[8] W.A. Algozeeb, P.E. Savas, D.X. Luong, W.Y. Chen, C. Kittrell, M. Bhat, R. Shahsavari, J.M. Tour, Flash graphene from plastic waste, Acs Nano 14 (11) (2020) 15595–15604, https://doi.org/10.1021/acsnano.0c06328.
[9] M.G. Stanford, K.V. Bets, D.X. Luong, P.A. Advincula, W.Y. Chen, J.T. Li, Z. Wang, E.A. McHugh, W.A. Algozeeb, B.I. Yakobson, J.M. Tour, Flash graphene morphologies, Acs Nano 14 (10) (2020) 13691–13699, https://doi.org/10.1021/acsnano.0c05900.
[10] B. Deng, D.X. Luong, Z. Wang, C. Kittrell, E.A. McHugh, J.M. Tour, Urban mining by flash Joule heating, Nat. Commun. 12 (1) (2021) 26038–26039, https://doi.org/10.1038/s41467-021-.
[11] K.M. Wyss, J.L. Beckham, W.Y. Chen, D.X. Luong, P. Hundi, S. Raghuraman, R. Shahsavari, J.M. Tour, Converting plastic waste pyrolysis ash into flash graphene, Carbon 174 (2021) 430–443, https://doi.org/10.1016/j.carbon.2020.12.063.
[12] Y.T. Liao, R.T. Zhu, W.J. Zhang, Z. Liu, H.Y. Zhu, Y. Sun, Ultrafast synthesis of novel coal-based graphene and its anticorrosion properties of epoxy/graphene nanocomposite coatings, Prog. Org. Coat. 184 (2023), https://doi.org/10.1016/j.porgcoat.2023.107859.
[13] P.A. Advincula, D.X. Luong, W.Y. Chen, S. Raghuraman, R. Shahsavari, J.M. Tour, Flash graphene from rubber waste, Carbon 178 (2021) 649–656, https://doi.org/10.1016/j.carbon.2021.03.020.
[14] P.F. Huang, R.T. Zhu, X.X. Zhang, W.J. Zhang, Effect of free radicals and electric field on preparation of coal pitch-derived graphene using flash Joule heating, Chem. Eng. J. 450 (2022), https://doi.org/10.1016/j.cej.2022.137999.
[15] N.H. Barbhuiya, A. Kumar, A. Singh, M.K. Chandel, C.J. Arnusch, J.M. Tour, S. P. Singh, The future of flash graphene for the sustainable management of solid waste, Acs Nano 15 (10) (2021) 15461–15470, https://doi.org/10.1021/acsnano.1c07571.
[16] Y.D. Xu, J.Q. Zeng, W. Chen, R.Y. Jin, B. Li, Z.H. Pan, A holistic review of cement composites reinforced with graphene oxide, Constr. Build. Mater. 171 (2018) 291–302, https://doi.org/10.1016/j.conbuildmat.2018.03.147.
[17] Y.L. Lin, H.J. Du, Graphene reinforced cement composites: a review, Constr. Build. Mater. 265 (2020), https://doi.org/10.1016/j.conbuildmat.2020.120312.
[18] W. He, J.W. Liang, J.H. Xu, Z.A. Jiao, N. Cui, J.S. Zhou, Nanoarchitectonics effect of few-layer graphene on the properties of cement mortar, Constr. Build. Mater. 349 (2022), https://doi.org/10.1016/j.conbuildmat.2022.128738.
[19] B.M. Wang, S. Deng, Effect and mechanism of graphene nanoplatelets on hydration reaction, mechanical properties and microstructure of cement composites, Constr. Build. Mater. 228 (2019), https://doi.org/10.1016/j.conbuildmat.2019.116720.
[20] J. Liu, L.X. Zhao, L. Chi, G. Luo, T. Li, S.Y. Cai, Effect of multilayer graphene oxide on the hydration and early mechanical strength of cement mortar in low temperature, Constr. Build. Mater. 364 (2023), https://doi.org/10.1016/j.conbuildmat.2022.129997.
[21] Y.P. Sheng, C.Y. Zhu, A. Abdulakeem, P.Z. Hu, Z.J. Ye, L.B. Wang, Z.F. Xue, L.Y. Li, Study on mechanical properties of graphene modified cement mortar, Fuller. Nanotub. Carbon Nanostruct. 31 (4) (2023) 364–379, https://doi.org/10.1080/1536383x.2022.2163993.
[22] D. Lu, X.M. Shi, J. Zhong, Nano-engineering the interfacial transition zone in cement composites with graphene oxide, Constr. Build. Mater. 356 (2022), https://doi.org/10.1016/j.conbuildmat.2022.129284.
[23] M. Cologna, B. Rashkova, R. Raj, Flash sintering of nanograin zirconia in < 5 s at 850 °C, J. Am. Ceram. Soc. 93 (11) (2010) 3556–3559, https://doi.org/10.1111/j.1551-2916.2010.04089.x.
[24] Y.H. Dong, I.W. Chen, Onset criterion for flash sintering, J. Am. Ceram. Soc. 98 (12) (2015) 3624–3627, https://doi.org/10.1111/jace.13866.
[25] Y.X. Du, A.J. Stevenson, D. Vernat, M. Diaz, D. Marinha, Estimating Joule heating and ionic conductivity during flash sintering of 8YSZ, J. Eur. Ceram. Soc. 36 (3) (2016) 749–759, https://doi.org/10.1016/j.jeurceramsoc.2015.10.037.
[26] Y.H. Dong, I.W. Chen, Onset criterion for flash sintering, J. Am. Ceram. Soc. 98 (12) (2015) 3624–3627, https://doi.org/10.1111/jace.13866.
[27] Y.Y. Zhang, J.I. Jung, J. Luo, Thermal runaway, flash sintering and asymmetrical microstructural development of ZnO and ZnO-Bi_2O_3 under direct currents, Acta Mater. 94 (2015) 87–100, https://doi.org/10.1016/j.actamat.2015.04.018.
[28] Z.Q. Tu, Z.C. Liu, Y.F. Li, F. Yang, L.Q. Zhang, Z. Zhao, C.M. Xu, S.F. Wu, H.W. Liu, H.T. Yang, P. Richard, Controllable growth of 1–7 layers of graphene by chemical vapour deposition, Carbon 73 (2014) 252–258, https://doi.org/10.1016/j.carbon.2014.02.061.
[29] J.A. Garlow, L.K. Barrett, L.J. Wu, K. Kisslinger, Y.M. Zhu, J.F. Pulecio, Large-area growth of turbostratic graphene on Ni(111) via physical vapor deposition, Sci. Rep. 6 (2016), https://doi.org/10.1038/srep19804.
[30] Y.H. Gao, W. Shi, W.C. Wang, Y. Wang, Y.P. Zhao, Z.H. Lei, R.R. Miao, Ultrasonic-assisted production of graphene with high yield in supercritical CO_2 and its high electrical conductivity film, Ind. Eng. Chem. Res. 53 (7) (2014) 2839–2845, https://doi.org/10.1021/ie402889s.
[31] D. Yoon, H. Moon, H. Cheong, J.S. Choi, J.A. Choi, B.H. Park, Variations in the Raman spectrum as a function of the number of graphene layers, J. Korean Phys. Soc. 55 (3) (2009) 1299–1303, https://doi.org/10.3938/jkps.55.1299.
[32] S. Kapoor, A. Jha, H. Ahmad, S.S. Islam, Avenue to large-scale production of graphene quantum dots from high-purity graphene sheets using laboratory-grade graphite electrodes, Acs Omega 5 (30) (2020) 18831–18841, https://doi.org/10.1021/acsomega.0c01993.

[33] X.N. Chen, X.H. Wang, D. Fang, A review on C1s XPS-spectra for some kinds of carbon materials, Fuller. Nanotub. Carbon Nanostruct. 28 (12) (2020) 1048–1058, https://doi.org/10.1080/1536383x.2020.1794851.
[34] H. Muramatsu, Y.A. Kim, K.S. Yang, R. Cruz-Silva, I. Toda, T. Yamada, M. Terrones, M. Endo, T. Hayashi, H. Saitoh, Rice husk-derived graphene with nano-sized domains and clean edges, Small 10 (14) (2014) 2766–2770, https://doi.org/10.1002/smll.201400017.
[35] H.J. Du, S.D. Pang, Enhancement of barrier properties of cement mortar with graphene nanoplatelet, Cem. Concr. Res. 76 (2015) 10–19, https://doi.org/10.1016/j.cemconres.2015.05.007.
[36] J.T. Liu, J.L. Fu, Y. Yang, C.P. Gu, Study on dispersion, mechanical and microstructure properties of cement paste incorporating graphene sheets, Constr. Build. Mater. 199 (2019) 1–11, https://doi.org/10.1016/j.conbuildmat.2018.12.006.
[37] Y. Gao, X.Y. Zhu, D.J. Corr, M.S. Konsta-Gdoutos, S.P. Shah, Characterization of the interfacial transition zone of CNF-reinforced cementitious composites, Cem. Concr. Compos. 99 (2019) 130–139, https://doi.org/10.1016/j.cemconcomp.2019.03.002.
[38] J.Z. Xiao, W.G. Li, Z.H. Sun, D.A. Lange, S.P. Shah, Properties of interfacial transition zones in recycled aggregate concrete tested by nanoindentation, Cem. Concr. Compos. 37 (2013) 276–292, https://doi.org/10.1016/j.cemconcomp.2013.01.006.
[39] X.Y. Zhu, Y. Gao, Z.W. Dai, D.J. Corr, S.P. Shah, Effect of interfacial transition zone on the Young's modulus of carbon nanofiber reinforced cement concrete, Cem. Concr. Res. 107 (2018) 49–63, https://doi.org/10.1016/j.cemconres.2018.02.014.
[40] J.W. Ying, Z.M. Xie, B.X. Chen, Z.J. Jiang, Z.Q. Tian, J.Z. Xiao, Multi-scale experimental studies on mechanical properties of three-dimensional porous graphene cementitious composite, Cem. Concr. Compos. 147 (2024), https://doi.org/10.1016/j.cemconcomp.2023.105412.